Power Electronics and Drives

Adaptive High-Frequency Injection-Based Sensorless Control for an Outer-Rotor PMaSynRM

Research Paper

Hande Nevin Kılıç[1,2,*] , Yusuf Öner[1]

[1]*Pamukkale University, Department of Electrical and Electronics Engineering, Denizli, Turkey*
[2]*OSTIM Technical University, Department of Electrical and Electronics Engineering, Ankara, Turkey*

Abstract: High-frequency signal injection (HFI) is widely used for sensorless motor control but has mostly been studied in machines with high saliency ratios. In outer-rotor permanent magnet-assisted synchronous reluctance motors (OR-PMaSynRMs), the external rotor extends the magnetic flux path and increases the symmetry of the reluctance barriers. This reduces the inductance difference between the dq-axes, thereby lowering the saliency and weakening the effectiveness of conventional HFI methods in position estimation. Hence, advanced sensorless control strategies are required for such motors. This study presents an adaptive HFI control strategy that combines frequency, amplitude and filter adaptation with a proposed voltage limiting mechanism. The algorithm has been experimentally implemented for the first time on an OR-PMaSynRM. The results confirm the applicability of the HFI technique to low-saliency motors and its ability to provide reliable and robust sensorless control.

Abbreviations : ADC: Analog-to-Digital Converter; BPF: Band-Pass Filter; IPMSM: Interior Permanent Magnet Synchronous Motor; OR: Outer Rotor; PC: Personal Computer; PI: Proportional–Integral; PLL: Phase-Locked Loop; PMSM: Permanent Magnet Synchronous Motor; PWM: Pulse Width Modulation; RMS: Root Mean Square; RMSE: Root Mean Square Error; RPM: Revolutions Per Minute; VAR: Volt–Ampere Reactive.

1. Introduction

The growing demand for efficient and reliable electric drives has intensified research on sensorless control techniques, which estimate rotor position from current and voltage measurements instead of physical sensors. Common approaches include the model reference adaptive system (MRAS), the extended Kalman filter (EKF), electromotive force (EMF) estimation and high-frequency signal injection (HFI). Each technique offers specific advantages depending on the motor topology and speed range (Belghazali et al., 2025; Janiszewski, 2023; Ran et al., 2025; Rodriguez-Montero et al., 2021; Sandre-Hernandez et al., 2019; Zuo et al., 2023). The HFI method is particularly effective at zero and low-to-medium speeds, as it injects a high-frequency signal into the stator windings and utilises the rotor's magnetic anisotropy to estimate position through current variations along the direct (d) and quadrature (q) axes. Field-oriented control (FOC) is typically employed as the main framework, enabling independent control of flux and torque components while enhancing HFI performance without direct position feedback (Ferdiansyah and Hanamoto, 2024;

* Email: hande.kilic@ostimteknik.edu.tr

Lu et al., 2022; Matsuo and Lipo, 1993; Prystupa et al., 2023; Wang et al., 2022, 2023). In several studies, interior-rotor permanent magnet-assisted synchronous reluctance motors (PMaSynRMs) have employed real-time automatic tuning of the band-pass filter (BPF) and continuous monitoring-based control of the estimated angle error to improve the accuracy of rotor position estimation (Akgul et al., 2022). Similarly, for synchronous reluctance motors (SynRMs), various approaches adapt the injection amplitude according to instantaneous load, stabilising current components and improving robustness (Chen et al., 2024b; Li et al., 2020). Furthermore, hybrid sensorless control structures combining adaptive HFI at low speeds with EMF-based models at higher speeds have enabled full-speed-range operation (Lu et al., 2018; Ohnuma et al., 2014). Nevertheless, such adaptive HFI strategies have not yet been investigated for outer-rotor permanent magnet-assisted synchronous reluctance motors (OR-PMaSynRMs).

PMaSynRM motors have attracted increasing interest due to their high efficiency, low rotor losses and suitability for sensorless control. By reducing magnet volume through reluctance torque production, they achieve cost and thermal advantages while maintaining adequate torque at low current levels, thereby improving overall efficiency (Jani and Jamnani, 2023; Zhao et al., 2025). The outer-rotor topology considered in this study increases torque with the rotor diameter, enhancing torque density per unit volume. However, the extended magnetic flux path in this configuration reduces the saliency ratio compared with interior-rotor machines, making current responses less distinctive for rotor position estimation in HFI-based methods and limiting their applicability (Bozkurt et al., 2021). To enable effective HFI implementation in OR-PMaSynRMs, adaptive mechanisms for frequency, amplitude and filtering are required. The amplitude adaptation approach dynamically adjusts the injected signal according to operating conditions. This method stabilises the high-frequency current response and improves position estimation accuracy, provided that the signal amplitude remains below the voltage saturation limit (Alberti et al., 2017; Kang and Lorenz, 2018; Setty et al., 2013; Tongxing et al., 2019). Adaptive frequency control, on the other hand, adjusts the injection frequency to prevent interference with the fundamental component and noise coupling. Several studies have proposed dynamic tuning strategies to optimise estimation accuracy (Lee et al., 2024; Pan et al., 2016). The adaptive adjustment of demodulation filter cut-off frequencies according to signal variations is also essential. Matching the filter cut-off with the injection frequency enables precise current separation, while proportional tuning minimises coupling with fundamental components and improves stability (Chen et al., 2024b; Sun et al., 2022). Since adaptive HFI performance depends on machine parameters, the strategy must be individually optimised for each motor. Although previously applied to other configurations, it has not yet been implemented in OR-PMaSynRMs. In this study, the injection parameters were experimentally identified for the target motor and drive system. Additionally, a voltage limiting mechanism was developed to prevent saturation by continuously monitoring the total voltage vector and dynamically rescaling its magnitude when the threshold is reached, thus maintaining signal integrity and enhancing position estimation accuracy.

The contributions of this study to the literature can be summarised as follows:

- The control parameters required for efficient and stable operation of the OR-PMaSynRM, previously unexamined using the HFI method, were experimentally identified and compared with similar approaches applied to other motor types.
- Under dynamic operating conditions, the injection frequency, amplitude and demodulation filter cut-off were adaptively tuned, and an HFI-based sensorless control algorithm was developed specifically for the OR-PMaSynRM.
- A novel active voltage limiting method was proposed to enhance position estimation accuracy. The developed scheme was experimentally implemented and its effectiveness was verified.

2. Structural Features and Limiting of the OR-PMaSynRM

Reluctance-based motors are promising candidates for sensorless control due to their simple structure, low losses and high efficiency (Mishra, 2023). Compared with conventional SynRM, PMaSynRMs achieve higher torque density and improved efficiency by utilising rotor-embedded magnets that enhance magnetic flux and enable the generation of both reluctance and magnet torque (Diao et al., 2023; Hsieh et al., 2022; Murataliyev et al., 2022).

For effective control design, it is essential to have a clear understanding of the motor's magnetic and electrical behaviour. The motor's behaviour can be characterised in the dq reference frame through voltage, flux and torque equations, and its equivalent circuit is shown in Figure 1.
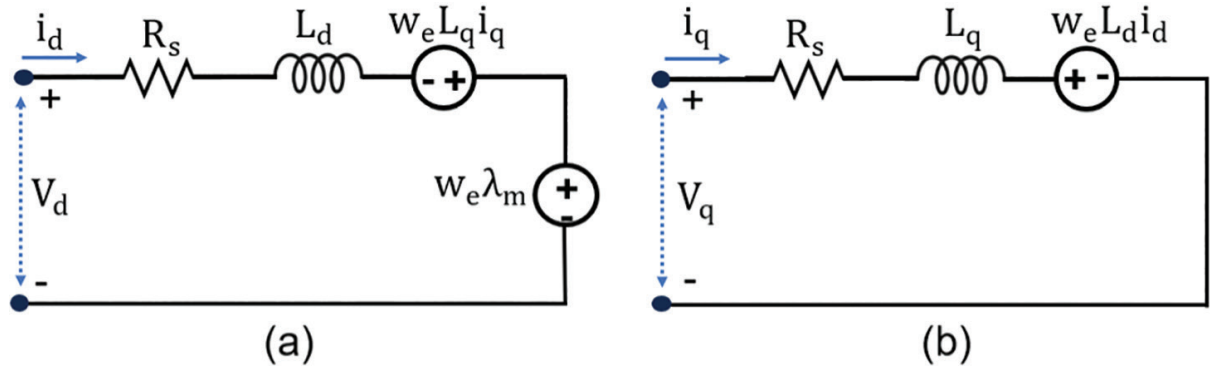
Figure 1. Equivalent electrical circuit representation of the OR-PMaSynRM in the dq reference frame: (a) d-axis model, (b) q-axis model. OR-PMaSynRM, outer-rotor permanent magnet-assisted synchronous reluctance motor.

In the equivalent circuit, R_s denotes the stator resistance, while L_d and L_q represent the dq-axis inductances, respectively. Based on this model, the electrical equations for the OR-PMaSynRM can be derived as follows:

$$V_d = R_s i_d + \frac{d\lambda_d}{dt} - \omega_e \lambda_q \tag{1}$$

$$V_q = R_s i_q + \frac{d\lambda_q}{dt} + \omega_e \lambda_d \tag{2}$$

In Eqs (1) and (2), V_d and V_q denote the stator voltages, i_d and i_q are the current components, λ_d and λ_q represent the flux linkages in the dq-axes and ω_e is the electrical angular speed of the rotor as follows:

$$\lambda_d = \lambda_d\left(i_d, i_q\right), \ \lambda_q = \lambda_q\left(i_d, i_q\right) \tag{3}$$

$$\lambda_q\left(i_d, i_q\right) = \lambda_{q0}\left(i_d, i_q\right) - \lambda_m \tag{4}$$

In Eq. (4), λ_q represents the total flux linkage along the q-axis, expressed as a non-linear function of the stator current components i_d and i_q. The term λ_{q0} denotes the q-axis flux linkage component that arises solely from the reluctance effect, excluding the influence of the permanent magnet flux. λ_m corresponds to the permanent magnet flux aligned with the q-axis. Under weak saliency, the reduced difference between L_d and L_q limits the distinctness of current responses, making rotor position estimation more difficult (Wu et al., 2017) as follows:

$$T = \frac{3}{2} P\left(\lambda_d i_q - \lambda_q i_d\right) + \lambda_{PM} i_q \tag{5}$$

In Eq. (5), the electromagnetic torque (T) comprises the reluctance torque, caused by the flux difference between the dq-axes, and the magnet torque, generated by the permanent magnets. Here, P denotes the number of poles, and λ_{PM} represents the magnet flux.

The structural comparison between the outer and inner rotor configurations is illustrated in Figure 2. Saliency refers to the difference in magnetic properties between the dq-axes of the motor and serves as an indicator of the magnetic anisotropy resulting from the rotor geometry. As the difference between the dq-axis inductances increases, the magnetic orientation disparity and the saliency level of the rotor become more pronounced.

Figure 3 shows the electromagnetic analysis of the OR-PMaSynRM. The motor's saliency ratio ($\xi = L_q/L_d$) is approximately 2.58, indicating low magnetic saliency. The reduced inductance difference ($L_d - L_q$) caused by the outer rotor design limits conventional sensorless control performance, especially at low and zero speeds. Although HFI relies on magnetic anisotropy for position estimation, weak current responses in low-saliency motors reduce accuracy and increase control complexity, requiring adaptive control strategies.
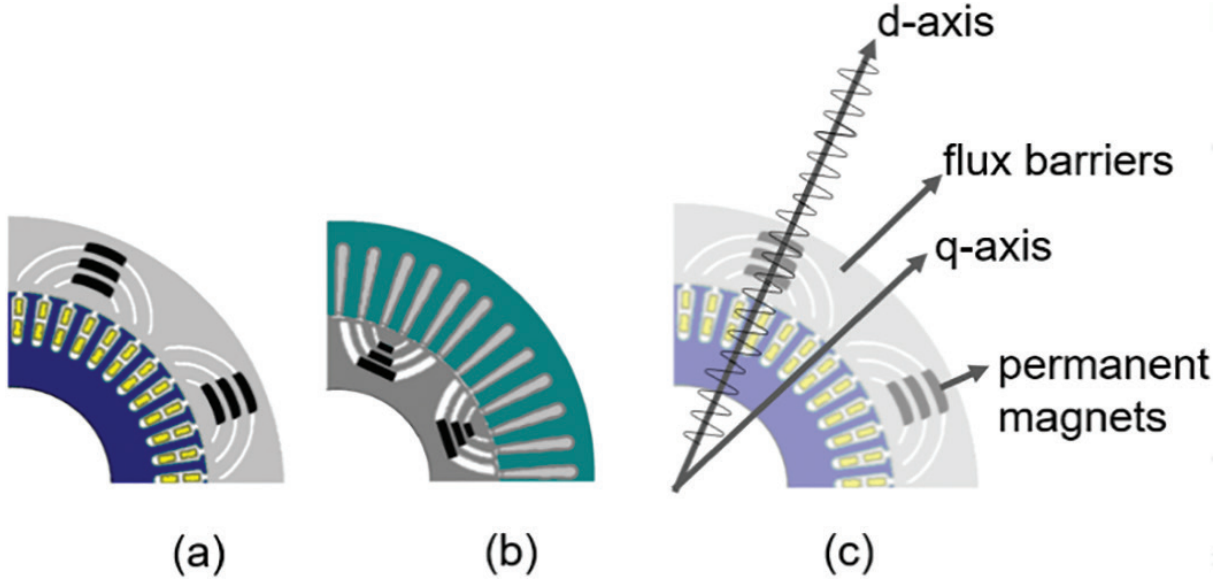
Figure 2. Cross-sectional views of PMaSynRM with (a) outer rotor and (b) inner rotor configurations. PMaSynRM, permanent magnet-assisted synchronous reluctance motors
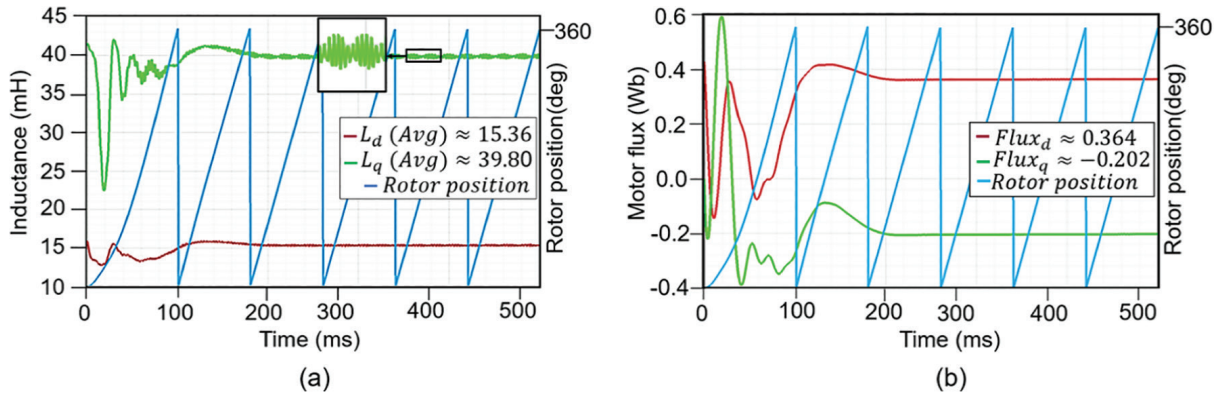
Figure 3. Electromagnetic characteristics of the OR-PMaSynRM: (a) Variation of the L_d and L_q inductances with respect to the rotor position and (b) magnetic flux linkage characteristics of the motor and the rotor position graph. OR-PMaSynRM, outer-rotor permanent magnet-assisted synchronous reluctance motor.

3. Adaptive High-Frequency Injection Modelling for the Outer-Rotor PMaSynRM

In HFI methods, the rotor position is estimated by applying a high-frequency voltage signal to the stator windings. The injected excitation interacts with the motor's intrinsic magnetic anisotropy and produces high-frequency current components whose amplitude and phase characteristics carry information related to the rotor position. In the conventional rotating-frame HFI approach, the high-frequency excitation is applied in the dq reference frame, thereby stimulating both axes simultaneously, and can be expressed as follows:

$$\begin{bmatrix} V_d^{\mathrm{HF}} \\ V_q^{\mathrm{HF}} \end{bmatrix} = V^{\mathrm{HF}} \begin{bmatrix} \sin(\omega_h t) \\ \cos(\omega_h t) \end{bmatrix} \tag{6}$$

In contrast, the pulsating HFI method adopted in this study injects the high-frequency voltage solely into the d-axis, while the q-axis component is kept at zero, and yields as follows:

$$V_d^{\mathrm{HF}} = V^{\mathrm{HF}} \sin(\omega_h t), \; V_q^{\mathrm{HF}} = 0 \tag{7}$$

This simplified d-axis injection is preferred because the d-axis aligns with the dominant saliency direction, resulting in a clearer and more distinguishable position dependent current response. Injecting a high-frequency signal into the q-axis, by contrast, would disrupt the torque producing current and increase torque ripple. Thus, d-axis pulsating excitation avoids such undesirable effects and offers clear advantages for OR-PMaSynRM machines, where saliency is naturally weaker. When the high-frequency voltage is applied to the d-axis, the measured currents include rotor position dependent high-frequency components (Jiang et al., 2024; Lu et al., 2021). In this context, the dq-axis high-frequency voltage components and the angular frequency of the injected signal are denoted by V_d^{HF}, V_q^{HF}, and ω_h, respectively; and since no high-frequency signal is applied to the q-axis in this study, the corresponding q-axis component remains zero. A demodulation stage is therefore required to extract these components and isolate the position information.

The phase currents (I_a, I_b, I_c) are processed through several stages, as shown in Figure 4. The measured currents are transformed into the stationary reference frame components (I_α, I_β) using the Clarke transformation. High-pass filter (HPF) is then applied to extract the high-frequency components, yielding the filtered signals $(I_{\alpha\beta}\mathrm{HPF})$. These signals are modulated with a sinusoidal reference to obtain the modulated currents $(I_{\alpha\beta}M)$. Finally, a low-pass filter (LPF) isolates the position-dependent component $(I_{\alpha\beta}\mathrm{LPF})$, which is used by the observer to estimate the rotor position (θ_{est}). Although this method is effective under certain conditions, its reliance on fixed signal parameters reduces stability under load variations and speed fluctuations. Therefore, adaptive HFI strategies based on frequency, amplitude and voltage adaptation have been developed to ensure reliable performance. The HPF removes the DC offset and low-frequency components of the measured current, allowing only the high-frequency components to pass through. The LPF, in turn, suppresses the high-frequency components and extracts the low-frequency signal containing rotor position information. This enhances the sensitivity of demodulation and maintains the stability of the estimated signal. Figures 5a and 5b show the discrete-time structures of the first-order digital HPF and LPF used in the demodulation stage.

3.1. Injected signal frequency adaptation in HFI

In HFI-based sensorless control, reliable extraction of rotor position-dependent current components necessitates adaptive adjustment of the signal parameters. Without proper adaptation, frequency mismatches may occur, leading to degraded estimation accuracy and reduced control performance as follows:

$$f_{\mathrm{HFI}}^{A} = f_{\mathrm{HFI,min}} + \frac{\mathrm{RPM}}{750}\left(f_{\mathrm{HFI,max}} - f_{\mathrm{HFI,min}}\right) \tag{8}$$

Eq. (8) presents the mathematical expression of the applied high-frequency adaptation. In this equation, f_{HFI}^{A} denotes the adaptive frequency, while $f_{\mathrm{HFI,min}}$ and $f_{\mathrm{HFI,max}}$ represent the lower and upper limits of the frequency adaptation, respectively. Furthermore, the equation defines the relationship between the adaptive frequency and the motor speed. In this study, the adaptive frequency mechanism is bounded by a maximum speed of 750 RPM, which corresponds to the rated mechanical speed of the OR-PMaSynRM used in the experiments. Since the operational speed range of the motor is limited to 0–750 RPM, the boundaries of the frequency adaptation have been defined in accordance with this mechanical operating interval. Figure 6 shows the flow of the adaptive high-frequency adjustment process based on motor speed.
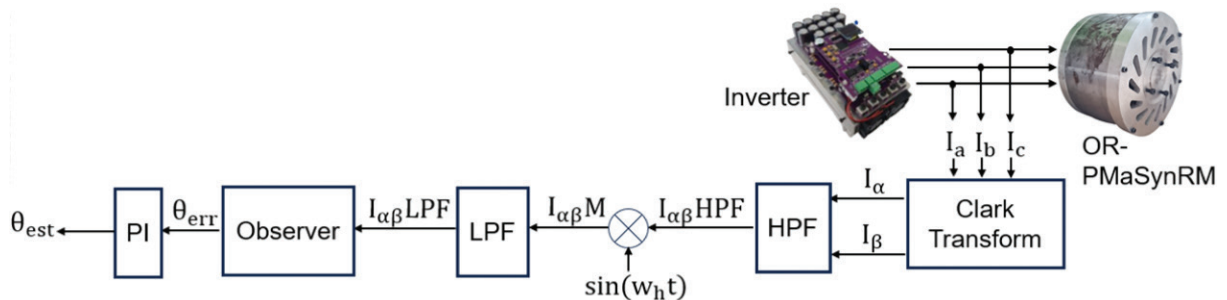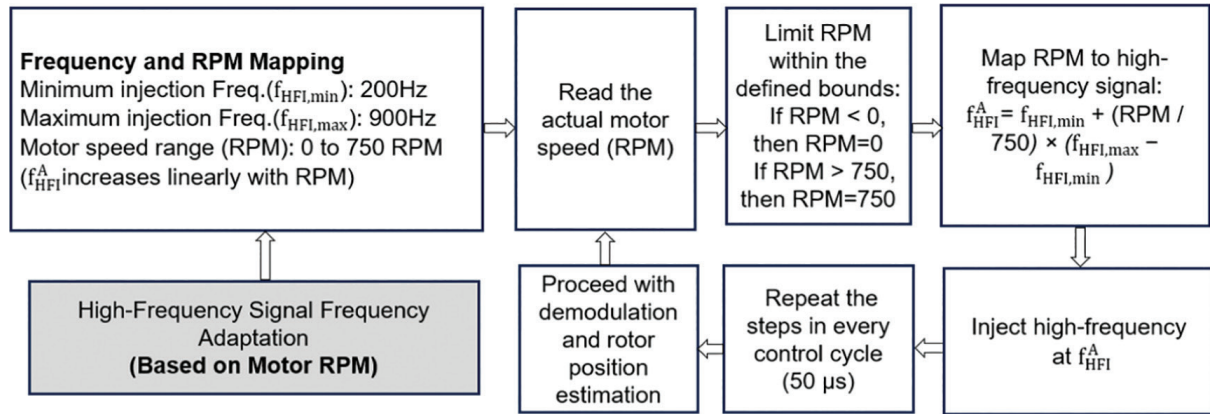

Figure 4. Demodulation stages in HFI-based rotor position estimation. HFI, high-frequency signal injection; HPF, high-pass filter; LPF, low-pass filter.
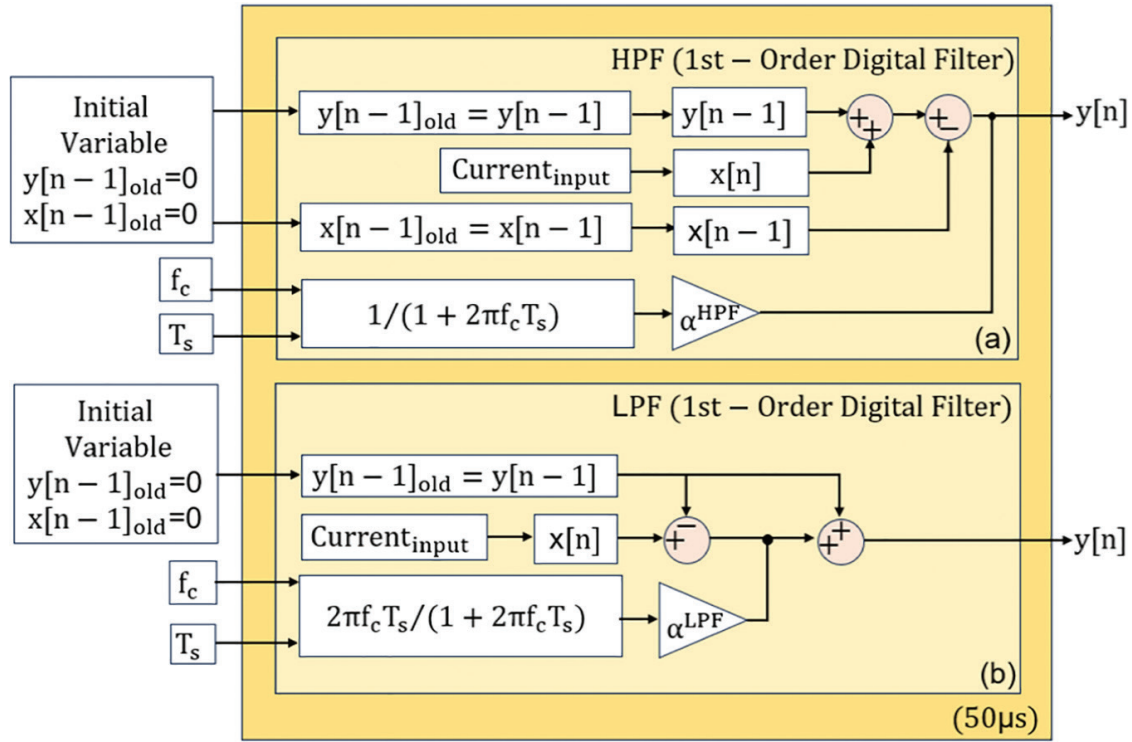
Figure 5. Implementation structures of the first-order digital filters: (a) HPF used in the demodulation stage, (b) LPF used in the signal extraction stage. HPF, high-pass filter; LPF, low-pass filter.

Figure 6. Flowchart of the adaptive frequency injection algorithm.

Although adaptive frequency enhances the separation of rotor-position-dependent components, it is not sufficient on its own. As the injection frequency varies, the cut-off frequencies of the HPF and LPF must also be adjusted accordingly. Otherwise, fixed filters cause spectral overlap, allowing unwanted components or attenuating relevant signals. Adaptive filtering, tuned according to motor speed and injection frequency, improves noise suppression at low speeds while preserving signal integrity at high speeds, thereby enhancing the reliability of rotor position estimation.

3.2. Injected signal amplitude adaptation of the HFI

Accurate extraction of current components containing rotor position information requires dynamic adjustment of the signal amplitude. A fixed amplitude, regardless of load or speed variations, may either weaken the injected signal or introduce noise under excessive levels. This condition reduces the accuracy of position estimation and negatively

affects overall system stability. Adaptive amplitude adjustment responds to these varying conditions, improving the signal-to-noise ratio and enhancing estimation accuracy as follows:

$$M_{\mathrm{HFI}}^{A} = M_{\mathrm{HFI,min}} + L_{\mathrm{ratio}} \left(M_{\mathrm{HFI,max}} - M_{\mathrm{HFI,min}} \right) \tag{9}$$

$$L_{\mathrm{ratio}} = \frac{\left| I_{\mathrm{means}} \right|}{I_{\mathrm{rated}}} \tag{10}$$

Eq. (9) presents the mathematical expression of the applied high-frequency signal amplitude adaptation. In this equation, M_{HFI}^{A} denotes the adaptive amplitude of the high-frequency signal, $M_{\mathrm{HFI,min}}$ represents the minimum adaptive amplitude limit, L_{ratio} indicates the load ratio and $M_{\mathrm{HFI,max}}$ defines the maximum amplitude limit. In Eq. (10), L_{ratio} represents the normalised load ratio, where I_{means} denotes the mean value of the measured motor phase current and I_{rated} is the rated full-load current. This ratio indicates the instantaneous motor load level and is used to proportionally adjust the injection amplitude within the defined limits.

Figure 7 shows the process flow of high-frequency signal amplitude adaptation based on motor load. The motor current is measured, the load ratio is calculated and the injection amplitude is adjusted in real time according to this ratio.

3.3. Proposed adaptive voltage limiting strategy for HFI in outer-rotor PMaSynRM drives

The key contribution of the proposed voltage-limiting structure lies in its ability to dynamically account for the additional voltage component arising from the adaptive nature of the HFI. Conventional voltage-limiting methods in the literature define the voltage boundary solely as a function of the DC-bus voltage and the fundamental FOC control action, implicitly assuming a constant-amplitude injection signal. In contrast, the HF amplitude in this study is adaptively varied in real time to enhance rotor-position estimation accuracy. As a result, classical limiting strategies become inadequate when the HF component increases the total voltage magnitude. The proposed method updates the voltage limit according to both the fundamental control terms and the instantaneous HF amplitude, ensuring that the V_{out} vector remains within the inverter boundaries and that the adaptive HFI mechanism operates stably. In this respect, the method provides a novel and necessary improvement over fixed-amplitude assumptions commonly adopted in prior work.

In the HFI strategy, maintaining the integrity of the injected signal is essential for accurate rotor position estimation. However, the inverter's DC bus limits the maximum output voltage, thereby constraining the total stator voltage vector (V_{out}). In adaptive HFI control, V_{out} consists of the d-axis component (V_d), the q-axis component (V_q) and the high-frequency signal (V_{HFI}) superimposed on the d-axis. Under high-load conditions, the combined magnitude of these components may exceed the DC bus limit, affecting system stability. To prevent this, a real-time adaptive voltage limiting strategy has been developed, ensuring that the V_{HFI} signal remains within safe voltage margins. This approach preserves both control stability and position estimation accuracy.
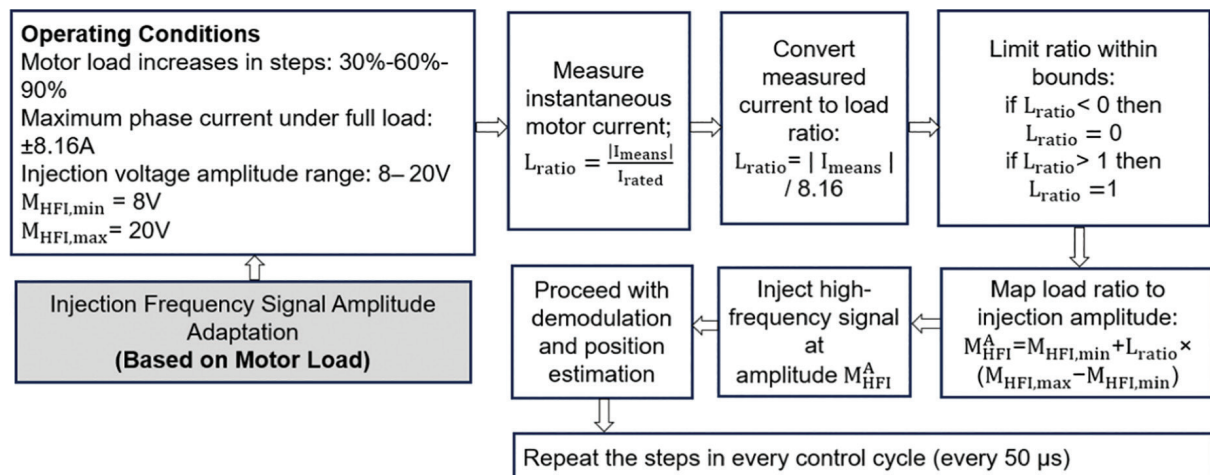
Figure 7. Flowchart of the adaptive injected signal amplitude control.

Figure 8 shows the effect of the proposed voltage-limiting strategy on V_{out} in the αβ (alpha–beta) reference frame. In Figure 8a, V_{HFI} is superimposed on the V_d component, and together with V_q, it forms the V_{out} vector. This vector exceeds the reference voltage boundary $\left(V_{\text{ref}}(\max)\right)$ defined by the inverter's DC-bus voltage (V_{in}). Exceeding this boundary reduces control accuracy and may lead to errors in rotor position estimation. Figure 8b illustrates the condition after applying the proposed voltage-limiting strategy. Once the overshoot is detected, the V_{out} vector is dynamically rescaled while preserving its phase angle. Consequently, a new vector, $V_{\text{out}}(\lim)$, is obtained within the permissible voltage region. The limited voltage components, $V_d(\lim)$ and $V_q(\lim)$, are recalculated to maintain the integrity of the superimposed V_{HFI} signal as follows:

$$V_{\text{out}} = \sqrt{V_d\text{total}^2 + V_q\text{total}^2} \tag{11}$$

$$V_{\text{ref}}(\max) = V_{in} x \frac{1}{\sqrt{3}} x 0.95 \tag{12}$$

$$\theta_v = \tan^{-1}\left(\frac{V_q\text{total}}{V_d\text{total}}\right) \tag{13}$$

Eqs (11)–(13) define the mathematical relationships used to calculate the total stator voltage magnitude, the inverter's maximum reference voltage and the phase angle of the voltage vector. Eq. (11) expresses the mathematical formulation of V_{out}, where $V_d$total corresponds to the sum of V_d and V_{HFI}, while V_q total corresponds to V_q. Eqs (12) and (13), respectively, provide the mathematical expressions for the maximum permissible reference voltage $V_{\text{ref}}(\max)$ and the phase angle θ_v, derived from the dq-axis voltage components.

Figure 9a presents a detailed vector representation of the proposed voltage limiting strategy, illustrating the error magnitude and corresponding correction mechanism when V_{out} exceeds $V_{\text{ref}}(\max)$. The V_d and V_q components combine with the V_{HFI} signal applied along the d-axis to form the total voltage vector V_{out}. When this vector surpasses $V_{\text{ref}}(\max)$, the exceeding portion is identified as the error vector (V_{Err}), defined by its magnitude and direction. This vector is decomposed into dq components, $V_{\text{Err}} \cdot \cos(\theta_v)$ and $V_{\text{Err}} \cdot \sin(\theta_v)$, which represent the excess voltage contributions along the respective dq-axes. These components are subtracted from the original voltage references to ensure that the resultant vector remains within the inverter's permissible range. Accordingly, the limited d-axis voltage $V_d(\lim)$ is obtained by subtracting $V_{\text{Err}} \cdot \cos(\theta_v)$ from $(V_d + V_{\text{HFI}})$, while the limited q-axis voltage $V_q(\lim)$ is derived by subtracting $V_{\text{Err}} \cdot \sin(\theta_v)$ from V_q. As a result, $V_{\text{out}}(\lim)$ is rescaled within the inverter voltage boundary while preserving its phase angle.

Figure 10a presents all parameters of the proposed adaptive HFI method in a block module form. As this module is part of the integrated control structure shown in Figure 12, its internal configuration is detailed here. Figure 10b illustrates the computational flow diagram of the proposed adaptive voltage limiting algorithm. This
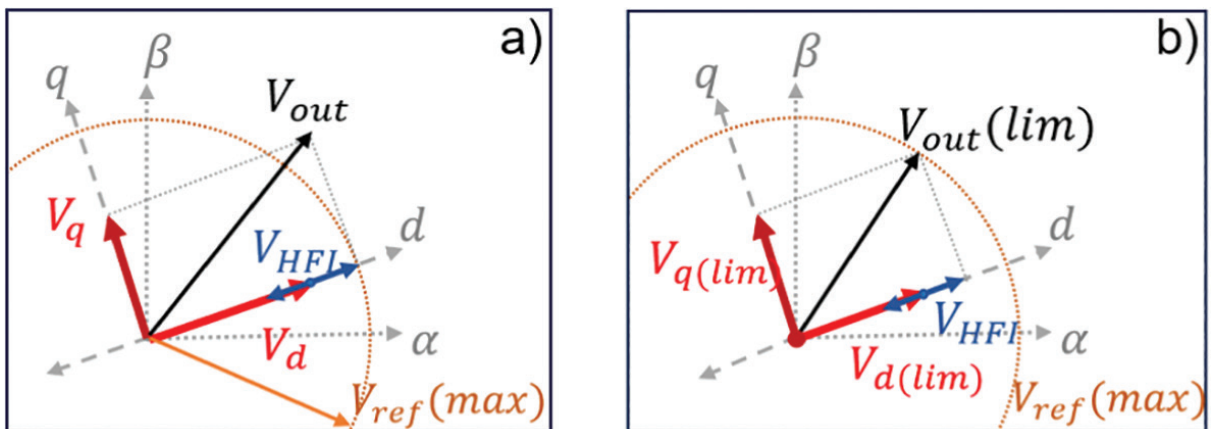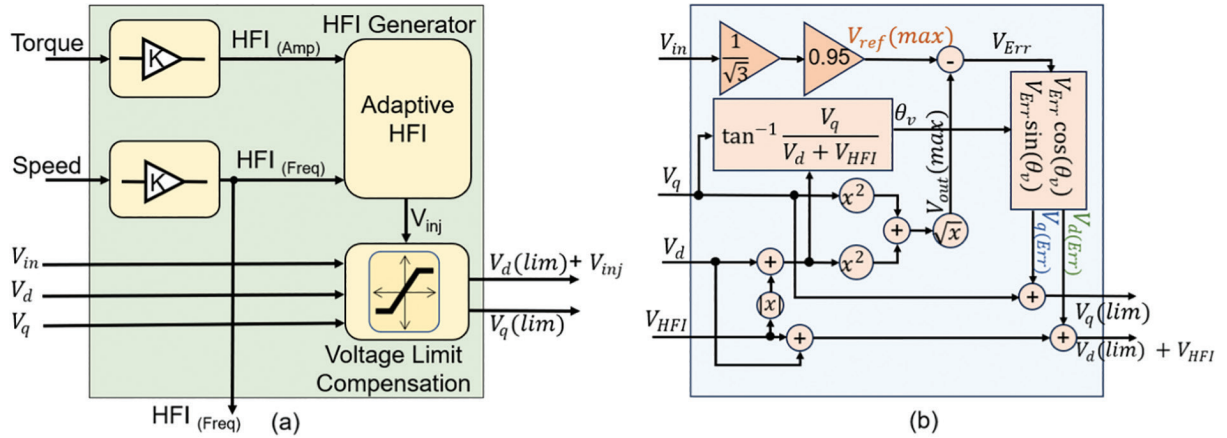

Figure 8. (a) Total stator voltage vector exceeding the voltage limit and (b) limited stator voltage vector.
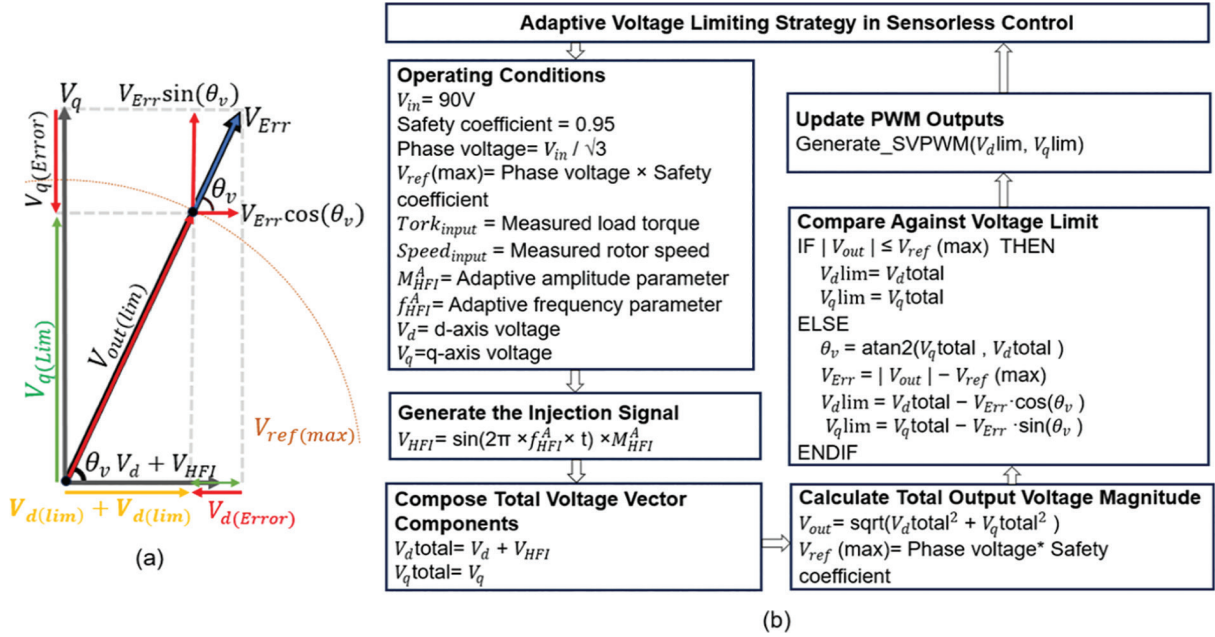
Figure 9. (a) Vector representation of the proposed limiting strategy based on error vector decomposition and (b) flowchart of the adaptive voltage limiting strategy. SVPWM, Space Vector Pulse Width Modulation.

Figure 10. (a) Adaptive HFI signal generation and voltage limiting block and (b) mathematical flow diagram. HFI, high-frequency signal injection.

diagram summarises the real-time mathematical processing steps performed to ensure that the total output voltage vector remains within the inverter's permissible range.

Figure 11 illustrates the dynamic behaviour of the output voltage components before and after activation of the voltage limiting strategy. During the initial interval ($t < t_0$), where t denotes the system time and t_0 represents the instant at which the strategy is enabled, the output voltage V_{out} periodically exceeds the inverter's permissible limit, generating the error voltage V_{Err}. This overflow distorts the trajectory of the voltage vector. As shown, the error components $V_d(Err)$ and $V_q(Err)$ represent the voltage overflow along the dq-axes and occur as a result of saturation. When the voltage limiting algorithm is activated at $t = t_0$, the voltage vector is dynamically reshaped and confined within the safe operating region defined by $V_{ref}(max)$. The dq-axis voltage components are updated in real time, resulting in the limited vectors $V_d(lim)$ and $V_q(lim)$. This process preserves the V_{HFI} signal applied on the d-axis, maintaining signal integrity and compatibility with the inverter's voltage capacity. Consequently, estimation stability is improved without transient distortion. The proposed voltage limiting structure enables the motor drive to operate within the inverter's voltage boundaries while preserving V_{HFI} signal integrity, thereby enhancing the accuracy and

reliability of sensorless rotor position estimation. The signal shown in Figure 11 was captured in real time from the computer interface connected to the operating motor drive.

Figure 12 illustrates the overall signal flow within the control structure. The difference between the reference and actual phase currents is processed by the PI controllers to generate the V_d and V_q components. These voltages, together with the reference speed, torque and $V_{ref}(max)$, are supplied to the block that performs adaptive HFI control and voltage limiting. Within this block, the adaptive HFI mechanism and the injected V_{HFI} signal generate the limited voltage components $V_d(\lim)$ and $V_q(\lim)$. These components are converted into V_a, V_b and V_c through inverse Park and Clarke transformations and are then applied to the Space Vector Pulse Width Modulation (SVPWM) module to produce the inverter switching signals. The adaptive HFI block dynamically adjusts the cut-off frequencies of the demodulation filters according to the injection frequency, thereby maintaining accurate signal extraction under varying operating conditions.
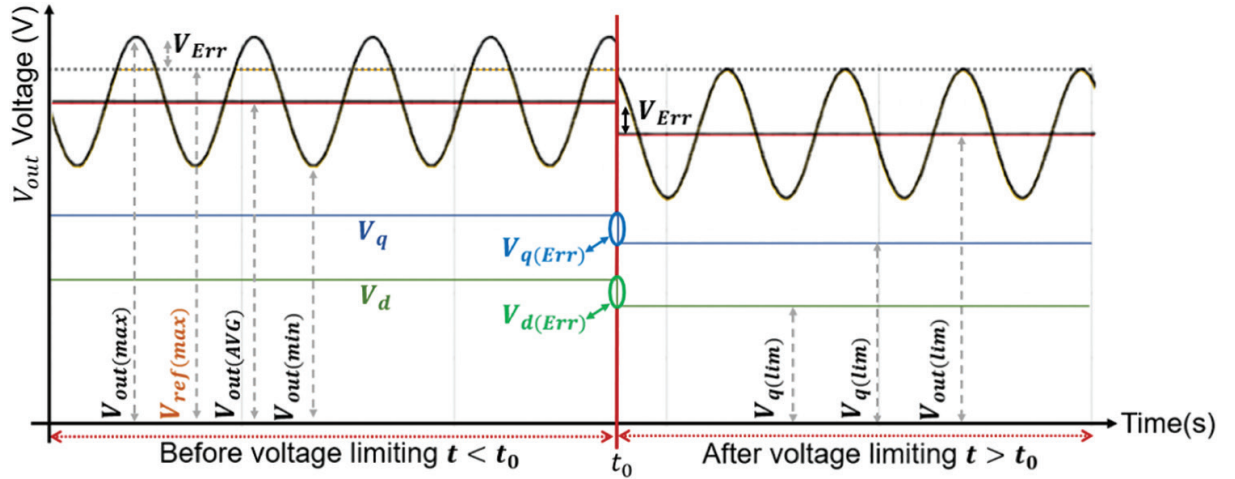

Figure 11. Comparison of the V_{HFI} signal integrity before and after the voltage limiting.
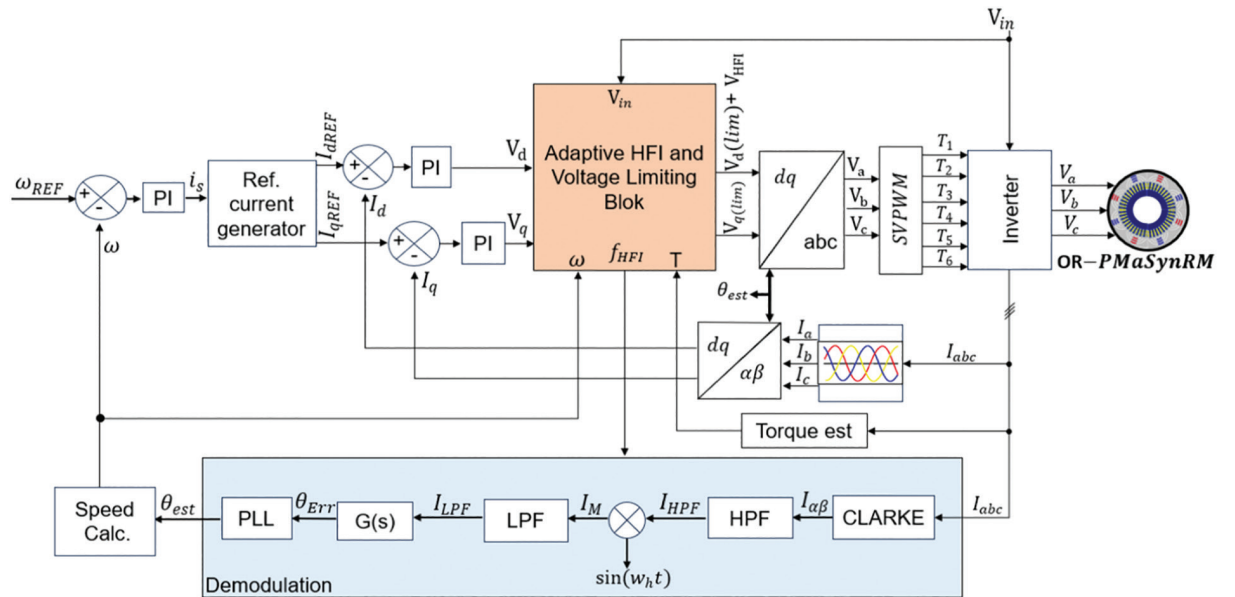

Figure 12. Block diagram of the FOC-based adaptive HFI sensorless control system. FOC, field-oriented control; HFI, high-frequency signal injection; HPF, high-pass filter; LPF, low-pass filter.

4. Experimental Results and Discussion

Figure 13 present the experimental set-up and schematic representation of the developed sensorless OR-PMaSynRM drive system. The DC power supply provides the input voltage to the inverter, while the motor drive circuit performs the control and switching operations. The isolated ST-Link programmer ensures electrical isolation between the computer and the system, allowing controller programming. The digital oscilloscope monitors system signals in real time, and the current probe measures the phase currents. The computer functions as both the control interface and the data acquisition unit. The loading unit enables testing of the motor under various load conditions.

During the experimental tests, the parameters of the hardware and software components forming the system are important. In this study, the data related to the hardware are summarised in Table 1, while the data related to the software are presented in Table 2. The limits of the adaptation parameters are listed in Table 3, and the technical parameters of the motor are provided in Table 4.

With its high processing capability and integrated peripherals, the STM32F407 microcontroller forms the core of the control architecture, providing a suitable structure for motor control applications. To reduce interference between the power and control stages, all digital signals are isolated through opto-isolators and isolated drivers. This hardware configuration provides a robust and noise-resilient platform for validating the proposed sensorless control under dynamic load conditions.

Based on the system parameters, several findings have been obtained from the experimental tests conducted to evaluate the performance of the adaptive HFI strategy. In this context, the responses observed during the frequency adaptation process reveal the system's dynamic behaviour and the accuracy of rotor position estimation. The experimental results related to frequency adaptation are presented in Figure 14.

Figure 14a illustrates the condition in which the injected signal frequency was kept constant while the motor speed was gradually increased from 0 RPM to 750 RPM, with no adaptive mechanism applied. As the speed increased, the stator current spectrum expanded, overlapping with both the HFI frequency band and the motor's inherent frequency components. Figure 14b, on the other hand, shows the adaptive adjustment of the injection frequency according to the motor speed. As the speed increased within the 0–750 RPM range, the injection frequency was updated based on experimentally determined threshold values. This approach preserved the integrity of rotor position-dependent information and improved demodulation accuracy. Following the frequency-adaptation stage, the motor speed was increased beyond its rated value to enable the transition into the flux-weakening region. This operating region is particularly important, as the reduction in effective magnetic flux at high speeds represents one
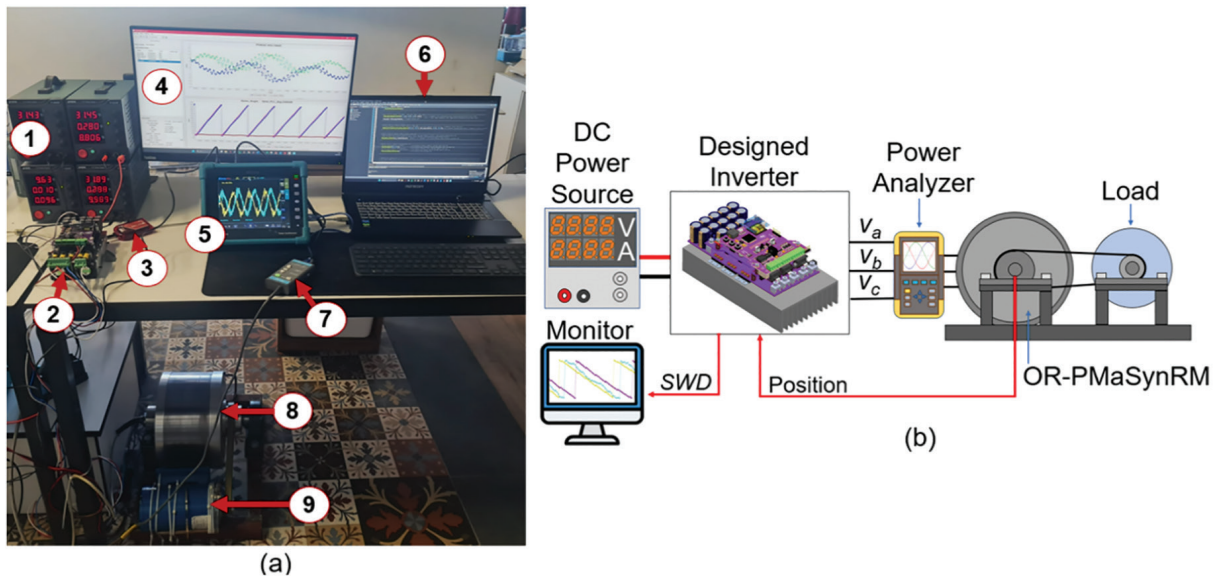
Figure 13. (a) The established OR-PmaSynRM sensorless drive system: (1) DC power source, (2) motor drive circuit, (3) isolated ST-Link, (4) monitor, (5) digital oscilloscope, (6) PC, (7) current probe, (8) OR-PMaSynRM, (9) current brake and (b) the OR-PMaSynRM drive test unit. OR-PMaSynRM, outer-rotor permanent magnet-assisted synchronous reluctance motor.

Table 1. Experimental hardware specifications.

Parameter	Value
Microcontroller	STM32F407VG (168 MHz, ARM Cortex-M4F [32-bit])
DC bus voltage (V_{in})	90 VDC
Current sensor type	GHS 20-SME
Current sensor output sensitivity	40 mV/A (typical)
Current sensing resolution	12-bit ADC
Position sensor (for validation only)	MA702, 14-bit magnetic encoder
Cooling method	Aluminium heatsink and fan

Table 2. Experimental software specifications.

Parameter	Value
Control method	FOC, HFI
HFI injection axis	d-axis only
Filter type (demodulation)	HPF and LPF (first-order digital)
Angle estimation method	PLL-based estimator with PI compensation
RMS angle error evaluation	RMSE
PWM switching frequency	15 kHz
Proportional and integral gain values for the d-axis current controller $\left(Kp_{id}^{p}, Ki_{id}^{p}\right)$	$Kp_{id}^{p} = 0.0005$, $Ki_{id}^{p} = 0.00075$
Proportional and integral gain values for the q-axis current controller $\left(Kp_{iq}^{p}, Ki_{iq}^{p}\right)$	$Kp_{iq}^{p} = 0.000001$, $Ki_{iq}^{p} = 0.0075$

FOC, field-oriented control; HFI, high-frequency signal injection; HPF, high-pass filter; LPF, low-pass filter.

**Table 3.** Boundaries of adaptive control parameters.

Control parameter	Adaptation variable	Operating range	Adaptive range
Adaptive injection frequency $\left(f_{HFI}^{A}\right)$	Motor speed (RPM)	0–750 RPM	200–900 Hz
Adaptive injection amplitude $\left(M_{HFI}^{A}\right)$	Load ratio (%)	30%–60%–90%	8–20 V
Adaptive filter cut-off frequency	f_{HFI}^{A}	–	200–900 Hz
Reference voltage limit $\left(V_{out(lim)}\right)$	$V_{d(Err)}, V_{q(Err)}$	–	45–49 V

Table 4. Specifications of the OR-PmaSynRM.

Parameter	Value	Unit
Phase voltage	90	V_{RMS}
Rated current	5.741	A_{RMS}
Reactive power	313	VAR
Output power	1500	W
Input power	1639	VA
Efficiency	91.51	%
Rated speed	750	RPM
Frequency	50	Hz
Load torque	19.1	Nm

OR-PMaSynRM, outer-rotor permanent magnet-assisted synchronous reluctance motor.
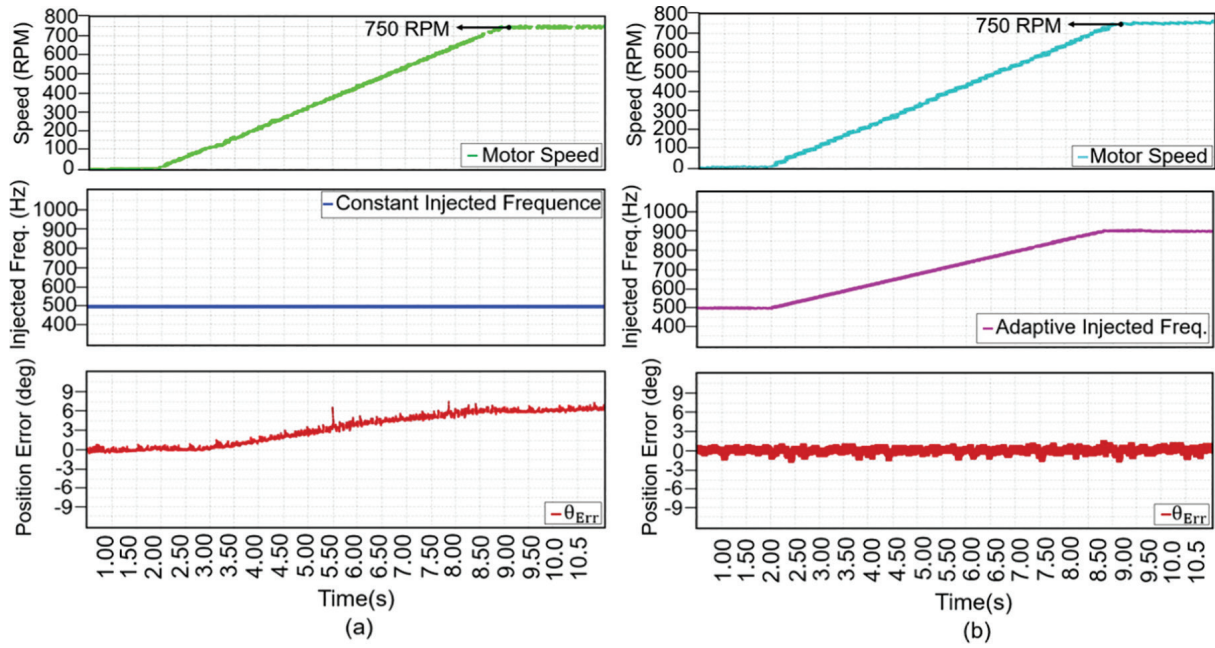
Figure 14. (a) Effect of a constant injection frequency on rotor position estimation error during motor speed increase and (b) impact of the adaptive injection signal frequency on rotor position estimation error during motor speed variations.

of the most challenging conditions for maintaining the accuracy of rotor-position estimation methods. Consequently, the proposed approach was evaluated under reduced-flux conditions to assess its estimation performance.

In the flux-weakening region, the OR-PmaSynRM continues to operate stably, while the electrical angle and torque characteristics exhibit the expected behaviour associated with the reduction in effective magnetic flux. The electrical angle between the rotor flux vector and the stator current vector is referred to as the torque angle, and the quantity shown as "Angle Degree" in Figure 15 corresponds to this torque angle. When the torque angle is increased, the motor enters the flux-weakening region, and a reduction in the available torque occurs due to the applied voltage and current limitations. The experimental results presented in Figure 15 demonstrate that rotor-position estimation maintains its integrity throughout this operating range.

Figure 16a shows a condition in which the motor was operated at different load levels (30%, 60%, and 90%) while the amplitude of the injected signal was kept constant. As the load increased, the fundamental components of the phase current became dominant, weakening the effect of the fixed-amplitude high-frequency signal and causing a noticeable rise in position error. This indicates that the constant-amplitude strategy cannot maintain stability under varying load conditions. Figure 16b presents the same test performed with an adaptive amplitude adjustment according to the motor torque. As the load increased, the injection signal amplitude was proportionally adjusted, preserving the saliency-related current components and improving demodulation accuracy. Consequently, the position estimation error was significantly reduced compared with the fixed-amplitude condition.

Figure 17 shows the motor phase current waveforms measured under HFI. When the waveforms are examined, the injected high-frequency components are clearly visible in the current.

Figure 18 shows the I_α and I_β current components obtained from the Clarke transformation of the phase currents. This operation represents the first step of the demodulation process. The resulting I_α and I_β currents contain high-frequency components superimposed on the fundamental current waveform.

Figure 19 illustrates the waveforms of I_αHPF and I_βHPF, corresponding to the αβ current components after high-pass filtering. At this stage, HPF is applied to the I_α and I_β signals to suppress the fundamental frequency components and extract the high-frequency content. As shown, the filtering process effectively eliminates the fundamental current component, thereby isolating the injected high-frequency signal for subsequent demodulation and position estimation.

Figure 20 illustrates the modulated current signals, denoted as $I_\alpha$mod and $I_\beta$mod, obtained through multiplication of the high-pass filtered currents with the injected high-frequency sine wave. During this modulation stage, the
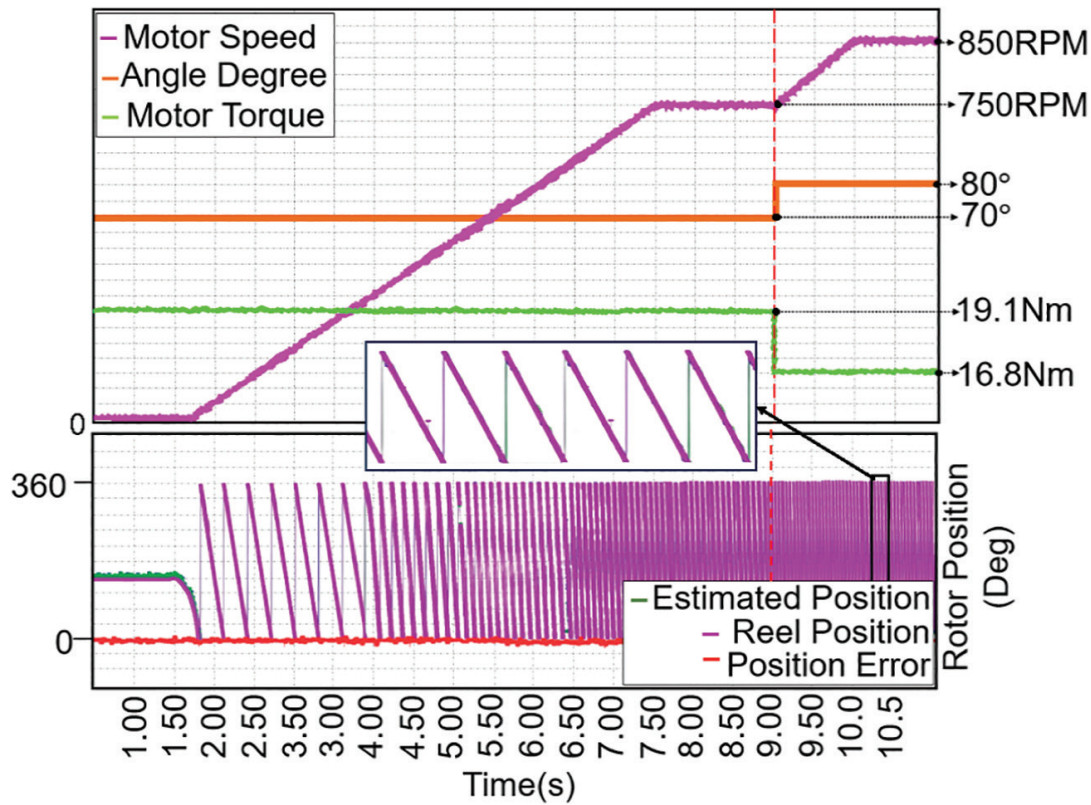
Figure 15. Flux weakening behaviour and rotor position estimation performance of the OR-PmaSynRM. OR-PMaSynRM, outer-rotor permanent magnet-assisted synchronous reluctance motor.
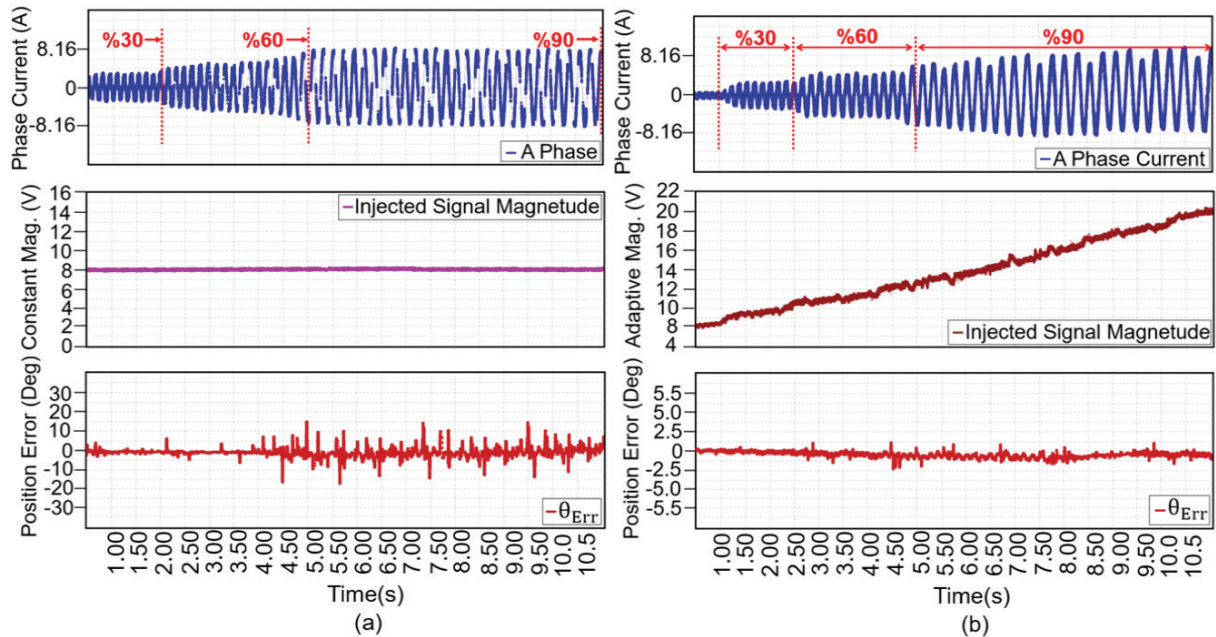
Figure 16. (a) Rotor position error resulting from a constant-amplitude injection signal under varying load conditions and (b) impact of the adaptive injection signal frequency on rotor position estimation error during motor speed variations.
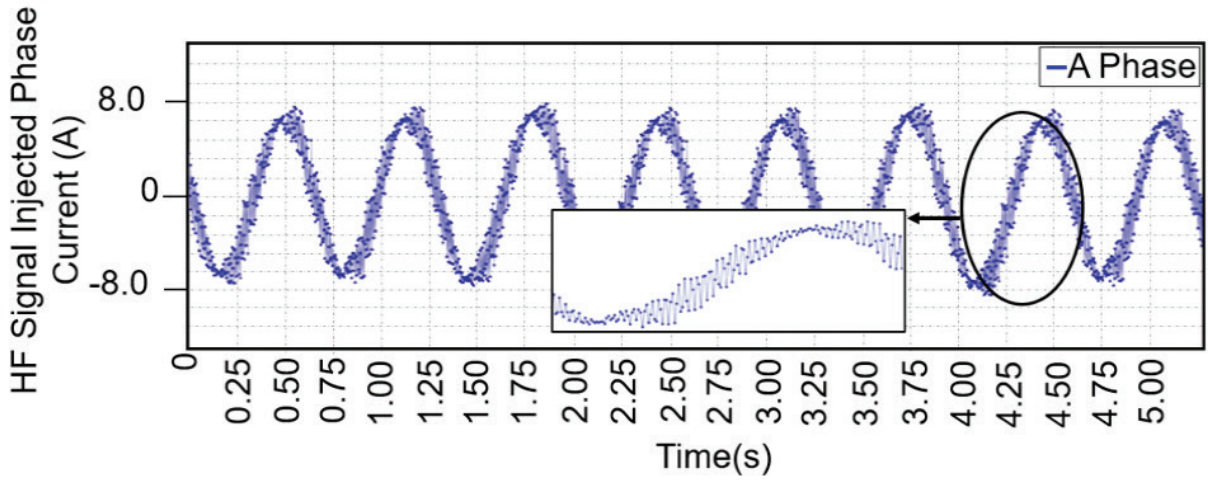
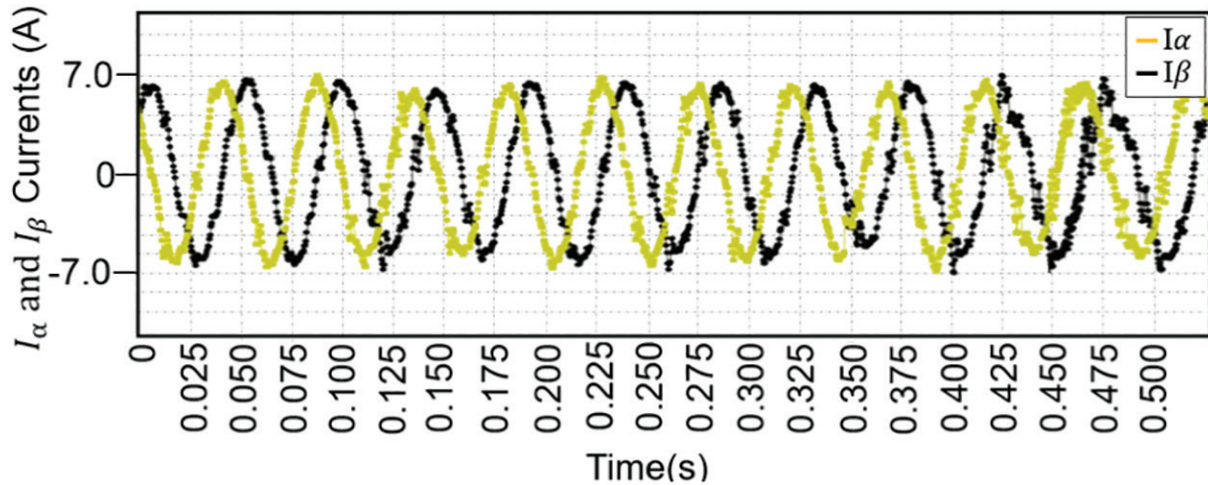**Figure 17.** Motor phase current under high-frequency injection.

Figure 18. I_α and I_β currents under high-frequency signal injection.

I_αHPF and I_βHPF components are synchronously multiplied by the same high-frequency carrier employed in the injection process. This operation enhances the saliency-related information and shifts the signal spectrum to a lower frequency band, thereby facilitating the subsequent demodulation stage.

Figure 21 presents the low-pass filtered current signals obtained following the modulation stage. In this stage, an LPF is applied to the $I_\alpha$mod and $I_\beta$mod signals to extract the low-frequency envelope that carries the rotor position information. This filtering operation effectively suppresses the high-frequency carrier components, producing smooth and sinusoidal current waveforms, as illustrated in the figure. The resulting signals, I_αLPF and I_βLPF, are then used for precise rotor angle estimation.

To evaluate the effectiveness of the proposed sensorless method, the estimated rotor position was compared with the actual position measured by a magnetic encoder. As shown in Figure 22a, the estimated position closely follows the actual one throughout the entire operating period. The position error was calculated as the difference between the estimated and encoder-measured positions and expressed in electrical degrees. In Figure 22b, the motor was decelerated to a standstill while rotating at 250 RPM and then accelerated again in the opposite direction. Within this operating range, the actual and estimated rotor positions, together with the position error, are presented. The error remains within ±1.15° (electrical degrees), indicating that the proposed HFI method accurately tracks the rotor position with minimal deviation.
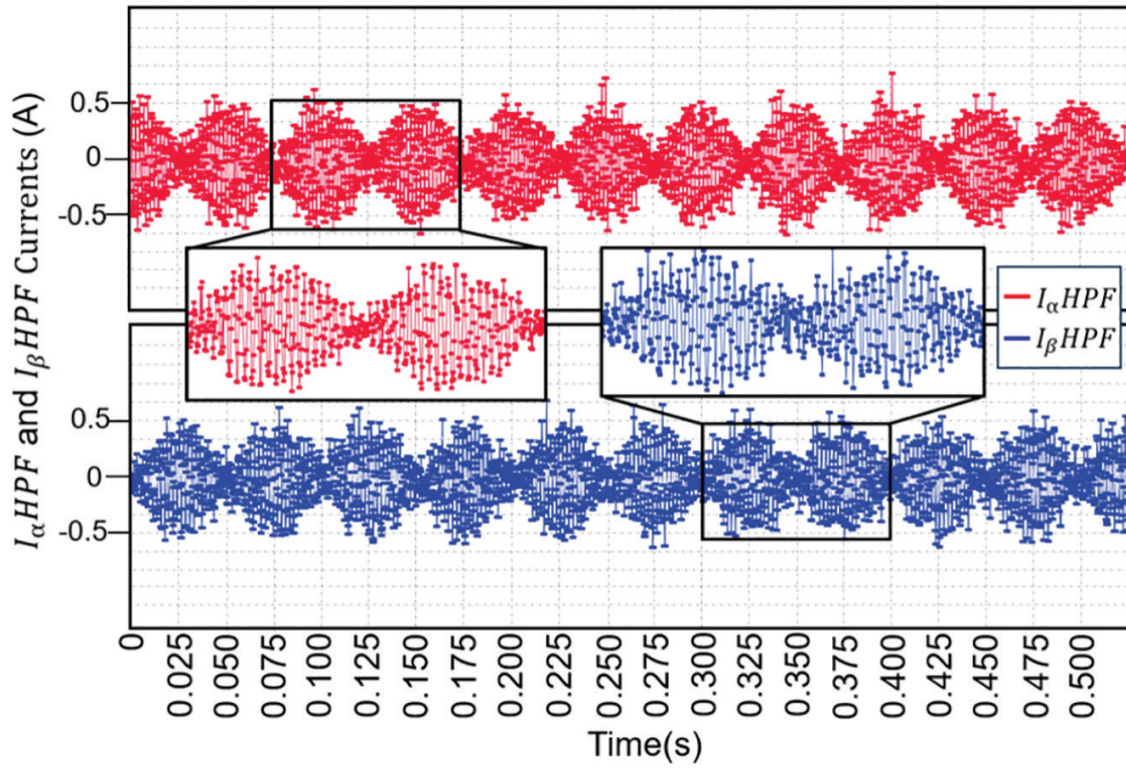
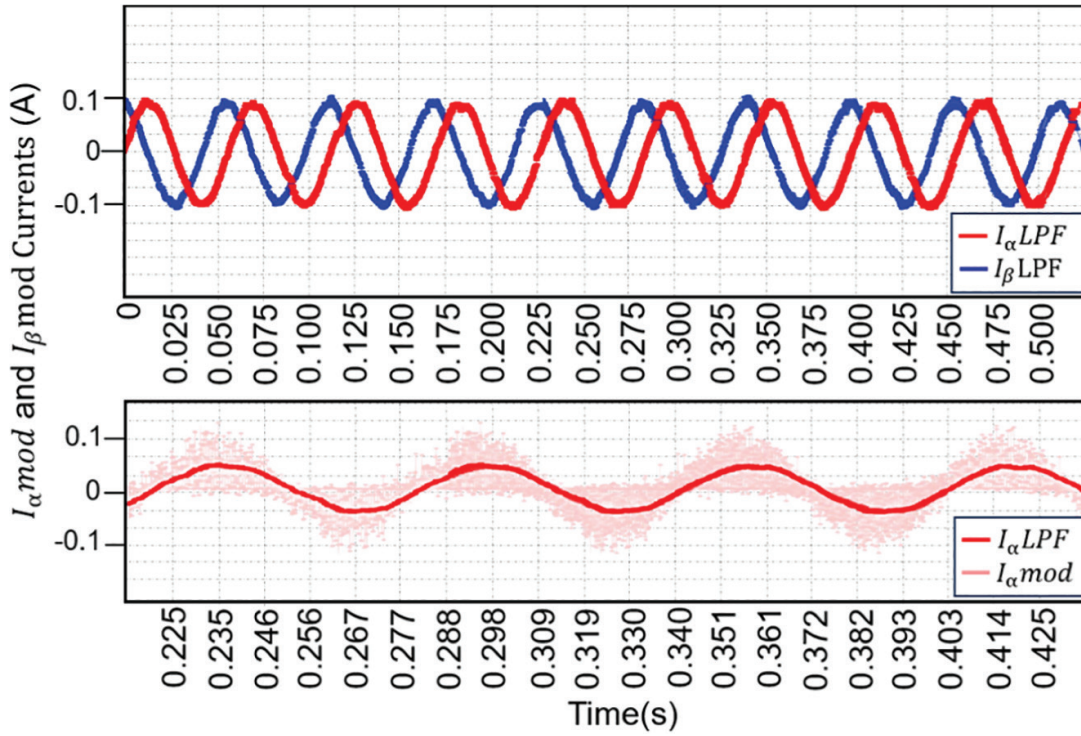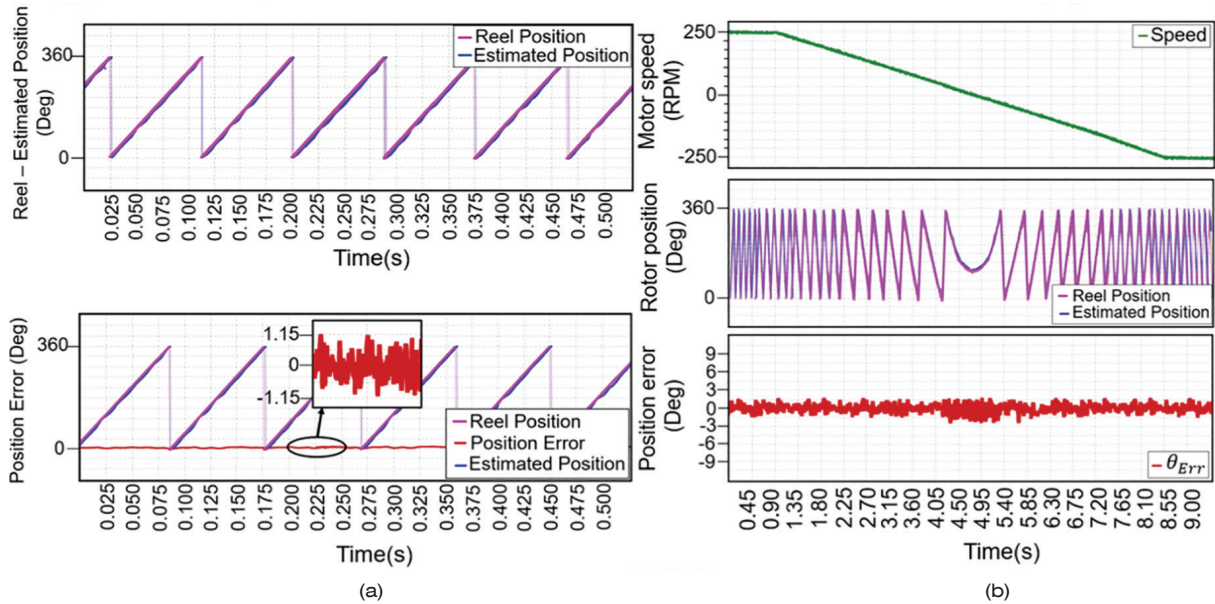**Figure 19.** I_{α}HPF and I_{α}HPF signals obtained after the HPF stage. HPF, high-pass filter.
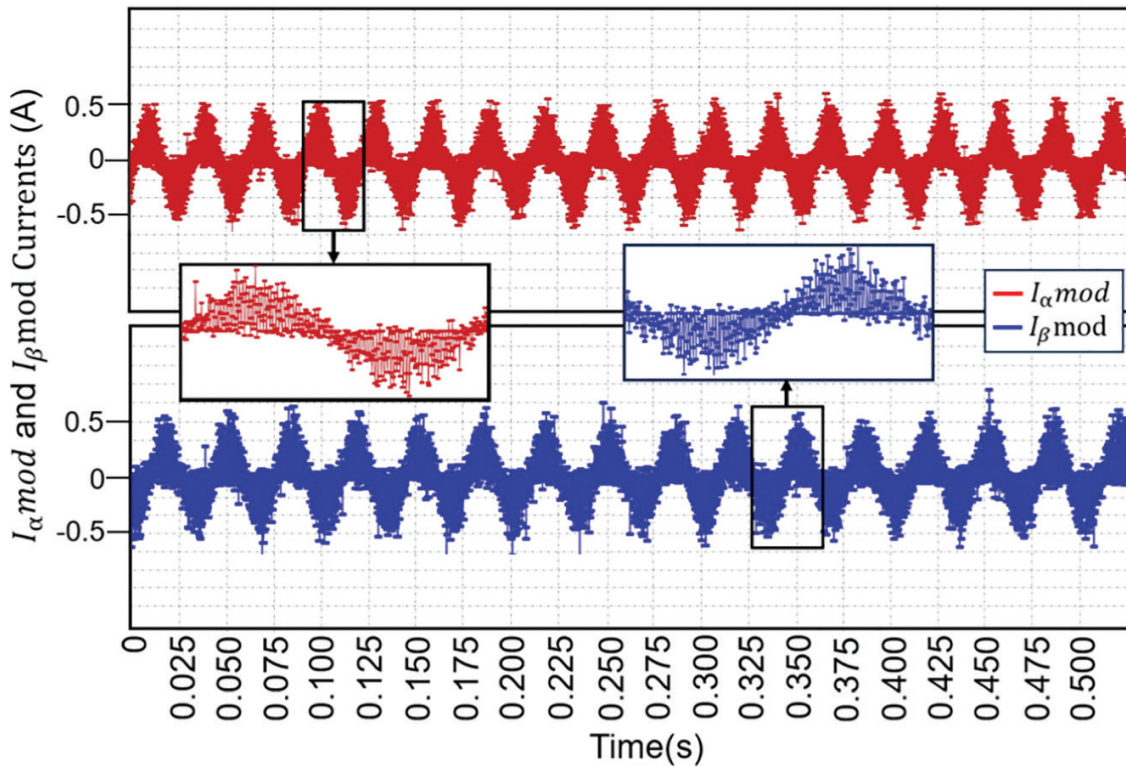
Figure 20. Outputs of I_{α}mod and I_{α}mod after sine-wave modulation.

Figure 21. $I_{\text{á}}$LPF and $I_{\text{á}}$LPF current outputs obtained after low-pass filtering. LPF, low-pass filter.

Figure 22. Rotor position estimation results: (a) Estimated rotor position compared with the real position and (b) rotor position estimation and corresponding error profiles under varying speed conditions.

Table 5 presents the RMS and maximum position estimation errors obtained under different operating conditions. The results show that the proposed adaptive HFI method provides stable and consistent estimation accuracy across the entire speed and load range. The RMS error remained approximately within ±1.15° electrical. Each experimental test was repeated three times under identical conditions to verify repeatability. The RMS position error values showed very small variation among trials, with the standard deviation ranging between ±0.02° and ±0.03°

electrical. Considering the repeated short-term tests and the measurement noise level, the deviation was confirmed to remain below approximately ±0.03° under nominal operating conditions.

During the rotor position estimation tests, additional experiments were conducted to further evaluate the performance of the proposed adaptive voltage limiting strategy. Figure 23 shows the system response with and without the voltage limiting enabled. The results demonstrate that rotor position estimation achieves higher accuracy, particularly during sudden load or speed variations. The signals were recorded in real time through the PC-based monitoring interface.

Figure 23 (top plot) shows the V_{out}, obtained as the sum of V_d and V_{inj} components. When the motor operates under load without the proposed limiting strategy, $V_{out}(max)$ exceeds the $V_{ref}(max)$ boundary, resulting in distortions in the $I_\alpha HPF$ and $I_\beta HPF$ signals. These distortions, visible in the middle section of Figure 23, adversely affect the accuracy of rotor position estimation. Upon activation of the proposed limiting strategy, a noticeable improvement in the estimated position signal was achieved.

Table 6 presents a comparison of sensorless rotor position estimation methods applied to different motor types under FOC control. While most existing studies have focused on inner-rotor motors, the method proposed in this study has been specifically developed for the OR-PmaSynRM, which exhibits weaker magnetic saliency. As adaptive HFI studies for outer-rotor configurations remain limited in the literature, most compared methods are based on inner-rotor motor types.

Table 5. RMS position error under different operating conditions.

Test condition	Motor speed (RPM)	Load torque (Nm)	RMS error (°electrical)	Standard deviation (°electrical)	Max error (°electrical)
Low speed, light load	150	≈5.7	1.10	±0.02	1.23
Medium speed, nominal load	450	≈11.5	1.12	±0.02	1.28
High speed, high load	750	≈17.2	1.15	±0.03	1.35
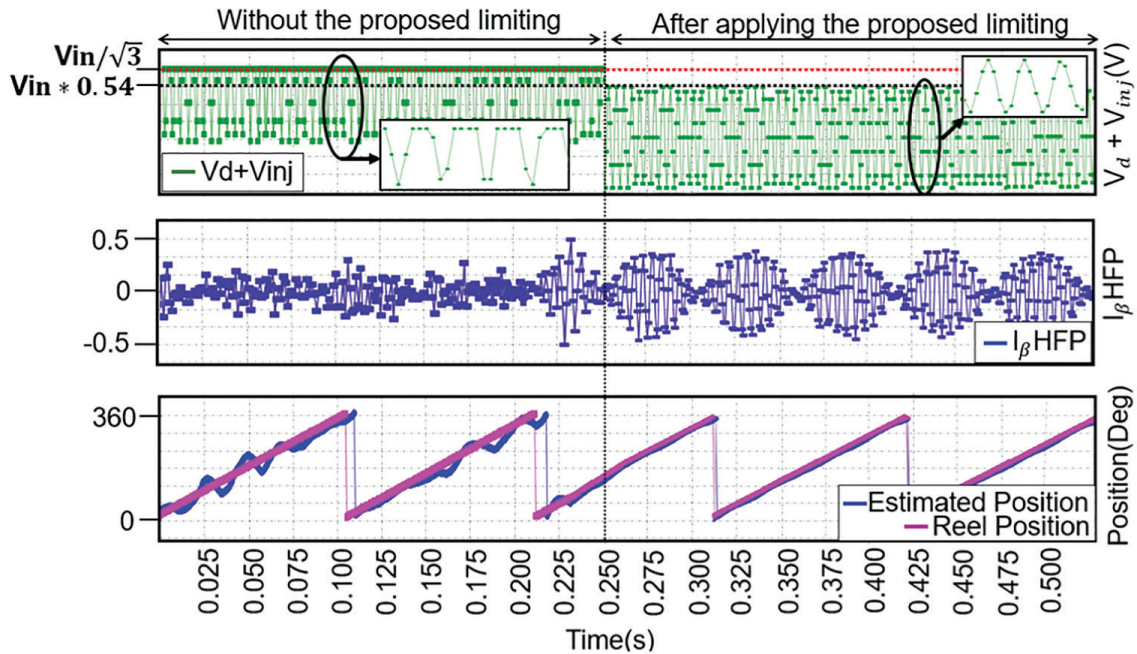
Figure 23. Impact of the proposed voltage limiting method on rotor position estimation.

Table 6. Comparison of rotor position estimation errors reported in various studies.

Study	Motor type	Control method	Estimation method	Average RMS error (electrical degrees)
Method in Chen et al. (2024a)	PMSM	FOC	Adaptive BPF + HFI	≈1.2°
Method in Tap et al. (2023)	PmaSynRM	FOC	Adaptive HFI + modified PLL	≈1°–1.5°
Method in Lu et al. (2018)	IPMSM	FOC	Adaptive frequency & amplitude HFI	<3°
Method in Chen and Liu (2012)	IPMSM	FOC	HFI	≈±2°
Method in Tongxing et al. (2019)	PMSM	FOC	Frequency self-optimized HFI + PLL	≈±14.4°
Method in Kumar et al. (2019)	IPMSM	FOC	HFI + Self-adaptive PLL + adaptive amplitude	≈1.5°
My work	OR-PmaSynRM	FOC	HFI + adaptive frequency + adaptive amplitude + proposed voltage limiting	±1.15°

FOC, field-oriented control; HFI, high-frequency signal injection; OR-PMaSynRM, outer-rotor permanent magnet-assisted synchronous reluctance motor; PMaSynRM, permanent magnet-assisted synchronous reluctance motors.

5. Conclusion

In this study, an HFI-based sensorless rotor position estimation method was proposed and experimentally implemented for OR-PMaSynRM drives. The proposed method dynamically adjusts the injection frequency (200–900 Hz), signal amplitude (8–20 V) and the cut-off frequencies of the demodulation filters (200–900 Hz) in real time according to the operating conditions. In addition, an adaptive voltage-limiting strategy was developed to ensure that the total voltage vector remains within the inverter's modulation capacity. Experimental results show that the proposed adaptive HFI algorithm significantly improves both position-estimation accuracy and control stability, particularly under low-speed and high-load conditions. The measured steady-state rotor position estimation error was obtained as an RMS value of approximately 1.15° electrical, with a standard deviation between ±0.02° and ±0.03° electrical. The maximum deviation remained below ±1.35° electrical throughout the entire speed range of 0–750 RPM. When the injection frequency or amplitude temporarily reached their adaptive limits, slight audible noise was observed in the motor, indicating that parameter adaptation is essential not only for maintaining estimation accuracy but also for preserving acoustic stability.

Acknowledgments

References

Akgul, K., Tap, A., Ergenc, A. F., Ergene, L. T. and Yilmaz, M. (2022). Sensorless control of PMaSynRM with HFI method using modified PLL for low speeds. *Proceedings of the IEEE International Conference on Electrical Machines (ICEM)*. Valencia, Spain, 5–8 September 2022.

Alberti, L., Bolognani, S., Zigliotto, M. and Petrella, R. (2017). Self-adaptive high-frequency injection-based sensorless control for IPMSM and SynRM. *Proceedings of the IEEE International Symposium on Sensorless Electric Drives (SLED)*. IEEE, Catania, Italy, pp. 97–102.

Belghazali, H. A., Abid, S., Cherif, H. and Mekhilef, S. (2025). Data-Driven Optimisation Method for Tuning the HF Injection Parameters of an Extra Low Voltage Encoderless Synchronous Motor Drive. *Power Electronics and Drives*, 10, pp. 1–10. doi: 10.2478/pead-2025-0022

Bozkurt, A., Oner, Y., Baba, A. F. and Ersoz, M. (2021). Design of external rotor permanent magnet synchronous reluctance motor (PMSynRM) for electric vehicles. In: Hemanth, J., Yigit, T., Patrut, B. and Angelopoulou, A. (eds) *Trends in Data Engineering Methods for Intelligent Systems (ICAIAME 2020)*. Lecture Notes on Data Engineering and Communications Technologies, vol. 76. Springer, Cham. doi: 10.1007/978-3-030-79357-9_38.

Chen, P., Ma, R., Song, S. and Chen, Z. (2024a). Adaptive filter based position estimation accuracy improvement for sensorless control of PMSM with high frequency voltage injection. *Proceedings of the IEEE Transportation Electrification Conference and Expo, Asia-Pacific (ITEC Asia-Pacific).* Xi'an, China, 28–31 May 2024, pp. 756–761.

Chen, J. L. and Liu, T. H. (2012). An IPMSM position control system using high frequency injection sensorless technique. *Proceedings of the IECON 2012 – 38th Annual Conference on IEEE Industrial Electronics Society.* Montreal, QC, Canada, pp. 3676–3681.

Chen, J., Chen, Q., Fan, Y. and Wang, Y. (2024). An amplitude-adaption high-frequency signal injection method for SynRMs at zero–low speed. *Journal of Electrical Engineering and Technology*, 19(5), pp. 3101–3109.

Diao, C., Zhao, B., Wang, T., Guo, Y. and Zhu, J. (2023). Permanent Magnet Assisted Synchronous Reluctance Motor With Asymmetric Rotor for High Torque Performance. *CES Transactions on Electrical Machines and Systems*, 7(2), pp. 179–186. doi: 10.30941/CESTEMS.2023.00016

Ferdiansyah, I. and Hanamoto, T. (2024). FPGA-Based High-Frequency Voltage Injection Sensorless Control With Novel Rotor Position Estimation Extraction for Permanent Magnet Synchronous Motor. *World Electric Vehicle Journal*, 15(11), p. 506. doi: 10.3390/wevj15110506

Hsieh, M. F., Lin, Y. K., Wu, T. H. and Chen, J. F. (2022). Flux Intensifying Feature of Permanent Magnet Assisted Synchronous Reluctance Motor With High Torque Density. *Electronics*, 11(3), p. 397. doi: 10.3390/electronics11030397

Jani, S. and Jamnani, J. (2023). Performance Validation of PM-Assisted SynRM and PMSM With Optimized Design for EV Application. *Transactions on Energy Systems Engineering and Applications*, 4(2), pp. 1–14. doi: 10.32397/tesea.vol4.n2.543

Janiszewski, D. (2023). Unscented Kalman Filter Sensorless Permanent Magnet Synchronous Motor Model Predictive Control. *Preprints (MDPI)*, 30 November 2023. doi: 10.20944/preprints202311.1907.v2

Jiang, D., Yang, L. and Cheng, M. (2024). An Improved Initial Rotor Position Estimation Method Using High-Frequency Pulsating Voltage Injection for PMSM. *Defence Technology*, 33, pp. 19–29. doi: 10.1016/j.dt.2023.07.020

Kumar, P., Petrella, R., Calligaro, S., Alberti, L. and Bottesi, O. (2019). Self-Adaptive High-Frequency Injection-Based Sensorless Control for Interior Permanent Magnet Synchronous Motor Drives. *Energies*, 12(19), p. 3645. doi: 10.3390/en12193645

Kang, Y.G., Lorenz, R.D., 2018. Using intentional magnetic saturation for HFI-based self-sensing with SPMSMs. In: IEEE International Conference on Power Electronics, Drives and Energy Systems (PEDES). Chennai, India, pp. 1–6, doi: 10.1109/PEDES.2018.8707698.

Lee, J. W., Kim, H. S., Park, J., Choi, H. and Moon, S. (2024). Common-Mode Voltage Reduction of Modular Multilevel Converter Using Adaptive High-Frequency Injection Method for Medium-Voltage Motor Drives. *Energies*, 17(6), p. 1367. doi: 10.3390/en17061367

Li, C., Zhang, G., Xu, D., Zhao, N. and Wang, G. (2020). Adaptive Pseudorandom High-Frequency Square-Wave Voltage Injection Based Sensorless Control for SynRM Drives. *IEEE Transactions on Power Electronics*, 36(3), pp. 3200–3210. doi: 10.1109/TPEL.2020.3015704

Lu, J., Liu, J., Hu, Y., Zhang, X., Ni, K., & Si, J. (2018). A Sensorless Rotor Position Estimation Scheme for IPMSM Using HF Signal Injection with Frequency and Amplitude Optimization. *Journal of Electrical Engineering & Technology*, 13(5), 1945–1955. doi: 10.5370/JEET.2018.13.5.1945

Lu, Q., Wang, Y., Mo, L., & Zhang, T. (2021). Pulsating high-frequency voltage injection strategy for sensorless permanent magnet synchronous motor drives. *IEEE Transactions on Applied Superconductivity*, 31(8), 1–4. https://doi.org/10.1109/TASC.2021.3094426

Lu, Q., Zhang, T., Mo, L., Gao, S. and Zheng, S. (2022). Rotor Position Estimation Strategy Based on Rotating High-Frequency Voltage Injection Using Synchronous Frequency Filter. *Applied Sciences*, 12(23), p. 11945. doi: 10.3390/app122311945

Matsuo, T. and Lipo, T. A. (1993). Current-sensorless field-oriented control of synchronous reluctance motor. *Proceedings of the IEEE Industry Applications Society Annual Meeting (IAS)*. Toronto, Canada, pp. 672–678. 3–8 October 1993. doi: 10.1109/IAS.1993.298879

Mishra, V. (2023). Emergence of synchronous reluctance motor drive for an electric vehicle. *Tuijin Jishu / Journal of Propulsion Technology*, 44(4), 4097–4103. doi: 10.52783/tjjpt.v44.i4.1622

Murataliyev, M., Staton, D., Mekhontsev, D., Semenov, D. and Gerada, C. (2022). Synchronous Reluctance Machines: A Comprehensive Review and Technology Comparison. *Proceedings of*

the *IEEE*, 110(3), pp. 382–399. doi: 10.1109/JPROC.2022.3145662

Ohnuma, T., Makaino, Y. and Saitoh, R. (2014). Adaptive signal injection method combined with EEMF-based position sensorless control of IPMSM drives. *Proceedings of the International Power Electronics Conference (IPEC)*. Hiroshima, Japan, pp. 914–918. 18–21. May 2014.

Pan, P. C., Tsai, M. C., Wang, J. W., Huang, T. J. and Hsieh, M. F. (2016). Adaptive Controller With an Improved High-Frequency Injection Technique for Sensorless Synchronous Reluctance Drive Systems. *IET Electric Power Applications*, 10(4), pp. 240–250. doi: 10.1049/iet-epa.2015.0304

Prystupa, D., Kocon, P., Polak, D., Mach, M., Kordylewski, M. and Mertens, A. (2023). Generalized High-Frequency Injection Framework for Sensorless Control of Synchronous Reluctance Machines. *IEEE Open Journal of the Industrial Electronics Society*, 4, pp. 304–315. doi: 10.1109/OJIES.2023.3298032

Ran, Y., Xia, Y., Qiao, M. and Sun, L. (2025). Review of Position Sensorless Control Technology for Permanent Magnet Synchronous Motors. *Energies*, 18(9), p. 2302. doi: 10.3390/en18092302

Rodriguez-Montero, E., Vogelsberger, M. and Wolbank, T. (2021). Initial Rotor Position Detection of Induction Machines Using Feedforward Sensorless Saliency Separation. *Power Electronics and Drives*, 6(41), pp. 301–313. doi: 10.2478/pead-2021-0020

Sandre-Hernandez, O., Cuvas-Castillo, C. and Ordaz-Oliver, P. (2019). Sensorless field oriented control of BLDC motor based on sliding mode observer. *Proceedings of the International Conference on Mechatronics, Electronics and Automotive Engineering (ICMEAE)*. Cuernavaca, Mexico, 6–8 November 2019, pp. 119–124.

Setty, A. R., Wekhande, S. and Chatterjee, K. (2013). Adaptive signal amplitude for high frequency signal injection based sensorless PMSM drives. *Proceedings of the IEEE International Symposium on Sensorless Control for Electrical Drives and Predictive Control of Electrical Drives and Power Electronics (SLED/PRECEDE)*. Munich, Germany, 17–19 June 2013, pp. 1–5.

Sun, J., Zhang, L., Liu, Z., Zhang, H., Wang, L. and Liu, G. (2022). Bandwidth and Audible Noise Improvement of Sensorless IPMSM Drives Based on Amplitude Modulation Multirandom Frequency Injection. *IEEE Transactions on Power Electronics*, 37(12), pp. 14126–14140. doi: 10.1109/TPEL.2022.3187535

Tap, A., Ergenc, A. F., Akgul, K., Ergene, L. T. and Yilmaz, M. (2023). A Lean Approach to Zero and Low-Speed Sensorless Control of PMaSynRMs. *IEEE Access*, 11, pp. 135406–135422. doi: 10.1109/access.2023.3337524

Tongxing, X., Xiaolin, W., Hang, Z. and Yuting, L. (2019). Position estimation method based on frequency self-optimization high-frequency signal injection. *Proceedings of the IEEE International Conference on Electrical Machines and Systems (ICEMS)*. Harbin, China, pp. 1–4. 11–14 August 2019.

Wang, X., Li, Y., Xiong, Z., Xie, W., Lin, X. and Jiang, H. (2023). Field-oriented control strategy for five-phase self-excited synchronous motor based on injecting high-frequency current. *Proceedings of the IEEE Industrial Electronics Conference (IECON)*. Singapore, pp. 1–6. 16–19 October 2023.

Wang, Z., Xiao, J., Lin, Z., Guo, Q., Chen, W. and Liang, T. (2022). High-Frequency Square-Wave Injection Sensorless Control Method of IPMSM Based on Oversampling Scheme. *World Electric Vehicle Journal*, 13(11), p. 217. doi: 10.3390/wevj13110217

Wu, W., Zhao, W., Zhang, X. and Xu, D. (2017). Design and Analysis of a Hybrid Permanent Magnet Assisted Synchronous Reluctance Motor Considering Magnetic Saliency and PM Usage. *IEEE Transactions on Applied Superconductivity*, 28(3), pp. 1–6. doi: 10.1109/TASC.2016.2633781

Zhao, M., Liu, G., Wang, X., Zhu, X., Mao, J. and Zheng, J. (2025). Fault-Tolerant Sensorless Control for a 3 × 3-Phase PMA-SynRM Based on Frequency-Adaptive Extended-State Observer. *IEEE Transactions on Transportation Electrification*, 11(1), pp. 2504–2515. doi: 10.1109/TTE.2024.3423479

Zuo, Y., Lai, C. and Iyer, K. L. V. (2023). A Review of Sliding Mode Observer-Based Sensorless Control Methods for PMSM Drives. *IEEE Transactions on Power Electronics*, 38(9), pp. 11352–11367. doi: 10.1109/TPEL.2023.3287828